Available online at www.sciencedirect.com
ScienceDirect
Trans. Nonferrous Met. Soc. China 35(2025) 1506−1516
Transactions of Nonferrous Metals Society of China
www.tnmsc.cn

Microstructure and mechanical properties of electron beam additively manufactured Ti−1Al−8V−5Fe alloy with different iron contents

Quan ZHOU[1,2,3], Xue-zhe ZHANG[2], Sheng-lu LU[3], Hui-ping TANG[2,4], Ma QIAN[3]

1. School of Materials Science and Engineering, Northeastern University, Shenyang 110819, China;
2. State Key Laboratory of Porous Metal Materials, Northwest Institute for Nonferrous Metal Research, Xi'an 710016, China;
3. Centre for Additive Manufacturing, School of Engineering, RMIT University, Melbourne, VIC 3000, Australia;
4. Advanced Materials Additive Manufacturing Research & Innovation Centre, Hangzhou City University, Hangzhou 310015, China

Received 8 October 2023; accepted 9 May 2024

Abstract: Ti−1Al−8V−5Fe (Ti-185) alloy with different iron contents was additively manufactured by electron beam powder bed fusion (EB-PBF), and its microstructure and mechanical properties were investigated. The results show that increasing the Fe powder content from 4.56 wt.% to 5.98 wt.% (within the specification range) converted coarse columnar prior-β grains in as-printed alloy into fine equiaxed ones ((54.2±32.4) μm) by EB-PBF. However, due to subsequent in-situ precipitation, a micron-thick low-solute weak α-phase became prevalent along each equiaxed grain boundary (GB). This drastically decreased the tensile deformation energy of Ti-185 from 6.2×10^7 J/m^3 (columnar grains) to 4.8×10^7 J/m^3 (equiaxed grains), despite a mild increase in strength. Fracture characteristics unveiled that the weak GB α-phase is the main crack initiation site and propagation path.

Key words: Ti−1Al−8V−5Fe alloy; equiaxed grain; deformation energy; grain boundary α; phase precipitation

1 Introduction

The metastable β-titanium alloy Ti−1Al−8V−5Fe (Ti-185, wt.%, the same below) was developed in the mid-1950s for aerospace fastener applications [1], with the specification of Ti−(0.8−1.5)Al−(7.5−8.5)V−(4−6)Fe−(≤0.5)O−(≤0.07)N−(≤0.05)C [2]. Ti-185 has the potential to achieve ultrahigh strength after precipitation hardening [3]. However, the severe microsegregation of Fe during ingot solidification, which leads to large Fe-stabilized β-fleck flaws [4], has long impeded its conventional manufacturing. Experimental studies on the effects of Fe-stabilized β-flecks in metastable β-titanium alloy Ti−10V−2Fe−3Al have shown that they can reduce tensile plasticity by more than 55% and low-cycle fatigue life by more than 90% [5].

Electron beam powder bed fusion (EB-PBF) additive manufacturing (AM) can effectively suppress the formation of Fe-stabilized β-flecks in Ti-185 [6] due to the microscale melt pool [7] and high solidification cooling rate [8]. Fe is the most powerful β-Ti stabilizer for Ti [9]. Compared with other commercial-grade Fe-containing Ti alloys [2], such as Ti−10V−2Fe−3Al (Ti-1023, (1.6−2.2)% Fe), Ti−3V−2Mo−4.5Al−2Fe (SP700, (1.7−2.3)% Fe) and Ti−6.8Mo−4.5Fe−1.5Al (TIMETAL LCB, (4.0−5.0)% Fe), Ti-185 allows for a wider range of Fe content specification from 4.0% to 6.0%. This is equivalent to varying the addition of V from 16% to 24% or the addition of Mo from 12% to 18% in Ti

Corresponding author: Hui-ping TANG, E-mail: thpz@hzcu.edu.cn; Ma QIAN, E-mail: ma.qian@rmit.edu.au
https://doi.org/10.1016/S1003-6326(25)66763-X

by the molybdenum equivalence [2]. In the latter case, laser powder deposited Ti−(12−18)Mo alloys exhibited a significant change in microstructure from Ti−12Mo to Ti−18Mo [10]. Furthermore, Fe is an effective growth-restriction solute for the solidification of prior-β grains in Ti [11]. For example, the addition of (3−5)% Fe to commercially pure Ti or Ti−6Al−4V can effectively refine the prior-β grains by laser-based AM [12−14]. Therefore, changing the Fe content from 4% to 6%, while still within the Fe specification range of Ti-185 alloy, may induce significant microstructural changes during and after solidification.

No experimental studies have been found to investigate the effects of Fe variations within the specification range on the microstructure and mechanical properties of Ti-185 alloy, including in conventional manufacturing. This study aims to reveal these potentially important effects by focusing on EB-PBF of Ti-185 alloy. Our findings provide insights into alloy design for AM and the selection of AM processes.

2 Experimental

The pre-alloyed spherical Ti-185 powder (Figs. 1(a, b)) was produced using a plasma rotation electrode process (PREP). The powder has the composition of Ti−1.38Al−8.0V−4.58Fe−0.15O−0.018N and is in the size range of 50−150 μm, with $D_{v(10)}$=73 μm, $D_{v(50)}$=109 μm and $D_{v(90)}$=142 μm. Its Fe content is close to the lower limit of the specification range. We then mixed the powder with soft Fe nanopowder (100 nm) to increase the Fe content to 6.0% by light ball milling. The powder remained spherical after the light ball milling, as shown in Figs. 1(c, d).

An EB-PBF system (Y150, Xi'an Sailong AM Technologies Co., Ltd., China) was used. Table 1 lists the parameters recommended by the system supplier for fabrication of high-quality Ti alloys with good productivity by EB-PBF. A bidirectional scan strategy was selected, which rotated 90° between layers. Rectangular coupons (80 mm ×

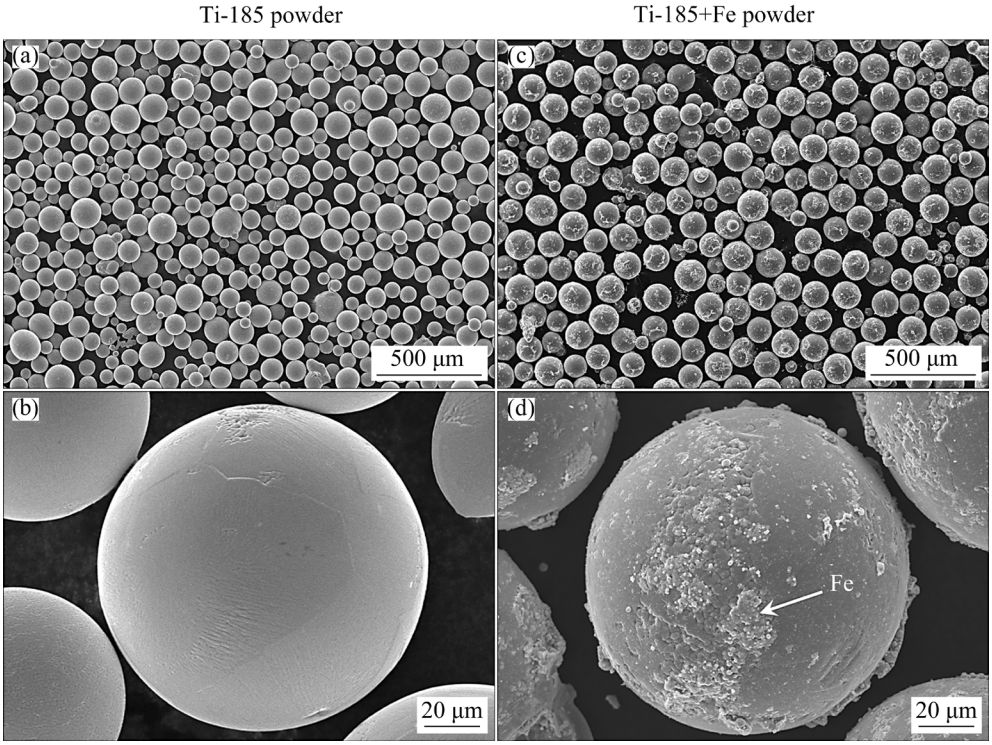

Fig. 1 Virgin spherical Ti−1.38Al−8.0V−4.58Fe−0.15O−0.018N powder before (a, b) and after coating with soft Fe nanopowder, containing nominal 6% Fe (c, d)

Table 1 EB-PBF parameters used for Ti-185 alloy

Acceleration voltage/kV	Fusion current/ mA	Scan speed/(m·s^{-1})	Hatch distance/μm	Layer thickness/μm	Preheating temperature/°C
60	15	3.3	100	100	720±10

12 mm × 20 mm; height: 20 mm) were printed on the 316L substrate plates. 316L was selected because it is more affordable and more accessible than Ti substrates. Furthermore, there is a practical reason, namely the interface between the 316L substrate and the Ti sample becomes brittle after EB-PBF. As such, the sample can be easily removed manually, without the need for wire cutting [15]. The brittleness stems from the formation of Fe- and Cr-containing intermetallic phases. On the other hand, at normal energy densities used in PBF AM, the influence of the substrate composition on PBF samples rarely goes beyond 0.5 mm, while the bottom 0.5−1.0 mm thick region is usually removed by post-processing in practice.

The alloy composition was analyzed using inductively coupled plasma optical emission spectrometry, where O and N contents were determined using an inert gas fusion analytical instrument (Leco-Tch600). Tensile coupons of two compositions were printed, Ti−1.33Al−7.86V−4.56Fe−0.13O−0.02N (Ti-185/4.56Fe) and Ti−1.32Al−7.96V−5.98Fe−0.13O−0.03N (Ti-185/5.98Fe).

Sample density was measured using the Archimedes method. X-ray diffraction (XRD, Bruker D8 Advance Phaser, Cu K_α radiation, λ=0.15406 nm), scanning electron microscopy (SEM, JEOL JSM−7200F) and transmission electron microscopy (TEM, FEI Talos F200X at 200 kV) with energy-dispersive X-ray spectroscopy (EDS) were used for detailed characterization. Microstructural texture was analyzed with electron backscatter diffraction (EBSD, Oxford Nordlys Max2), operated at 20 kV with a step size of 4 μm.

Tensile specimens with gauge dimensions of 25 mm × 6 mm × 2 mm were machined from the coupons, as per ASTM E8. Uniaxial tensile testing was performed on an Instron 5967 test machine with a constant strain rate of 1×10^{-3} s^{-1} at room temperature.

3 Results

3.1 Phase constituents and prior-β grain structures

XRD characterization (Fig. 2) revealed that the virgin powder contained only the β-phase while the two printed alloys contained both α and β phases. This indicates that in-situ α-phase precipitation occurred during EB-PBF.

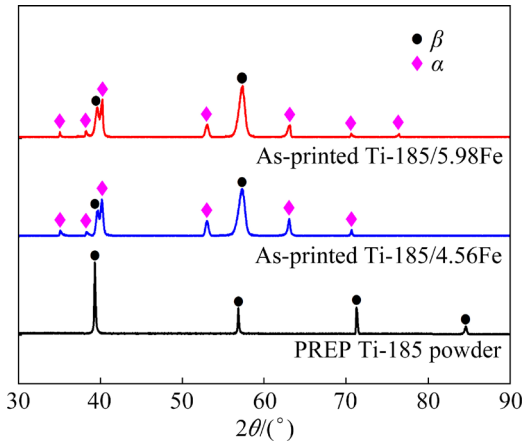

Fig. 2 XRD patterns of PREP Ti-185 powder and EB-PBF-printed Ti-185/4.56Fe and Ti-185/5.98Fe alloys

The as-printed Ti-185/4.56Fe alloy achieved a density of (4.693±0.02) g/cm^3 versus 4.695 g/cm^3 in its forged condition. Indeed, no pores or lack-of-fusion defects were observed in the microstructure (Fig. 3(a)). A similar situation was also observed for Ti-185/5.98Fe (Fig. 3(d)). However, a radical change occurred in the prior-β grain morphology and size, from coarse columnar Ti-185/4.56Fe (Fig. 3(b)) to fine equiaxed Ti-185/5.98Fe (Fig. 3(e)). No Fe-stabilized β-flecks were identified in each alloy (Figs. 3(c, f)), consistent with previous observations [6]. In fact, recent work has shown that binary Ti−Fe alloys containing up to 7% Fe can still avoid the formation of β-flecks via laser metal powder deposition [16], where the simulated solidification cooling rate (10^3–10^4 °C/s) is comparable to that of the EB-PBF process (10^3–10^5 °C/s [15]).

The inverse pole figure (IPF) maps confirmed the change from coarse columnar prior-β grains (up to 350 μm wide) in Ti-185/4.56Fe (Fig. 4(a)) to fine equiaxed ones ((54.2±32.4) μm) in Ti-185/5.98Fe (Fig. 4(d)). The maximum multiples of uniform distribution decreased from 31.8 (Fig. 4(b)) to 6.0 (Fig. 4(e)). Furthermore, the proportion of misorientation angles less than 10° dropped from 17% (Fig. 4(c)) to 2% (Fig. 4(f)). These EBSD data substantiated the change in texture.

Although Fe is known to promote the columnar-to-equiaxed transition (CET) in Ti alloys [14,17], this should be the first time that a small increase in Fe content (4.56% to 5.98%) leads to such a drastic change in the prior-β grain morphology and size. It is also worth noting that the

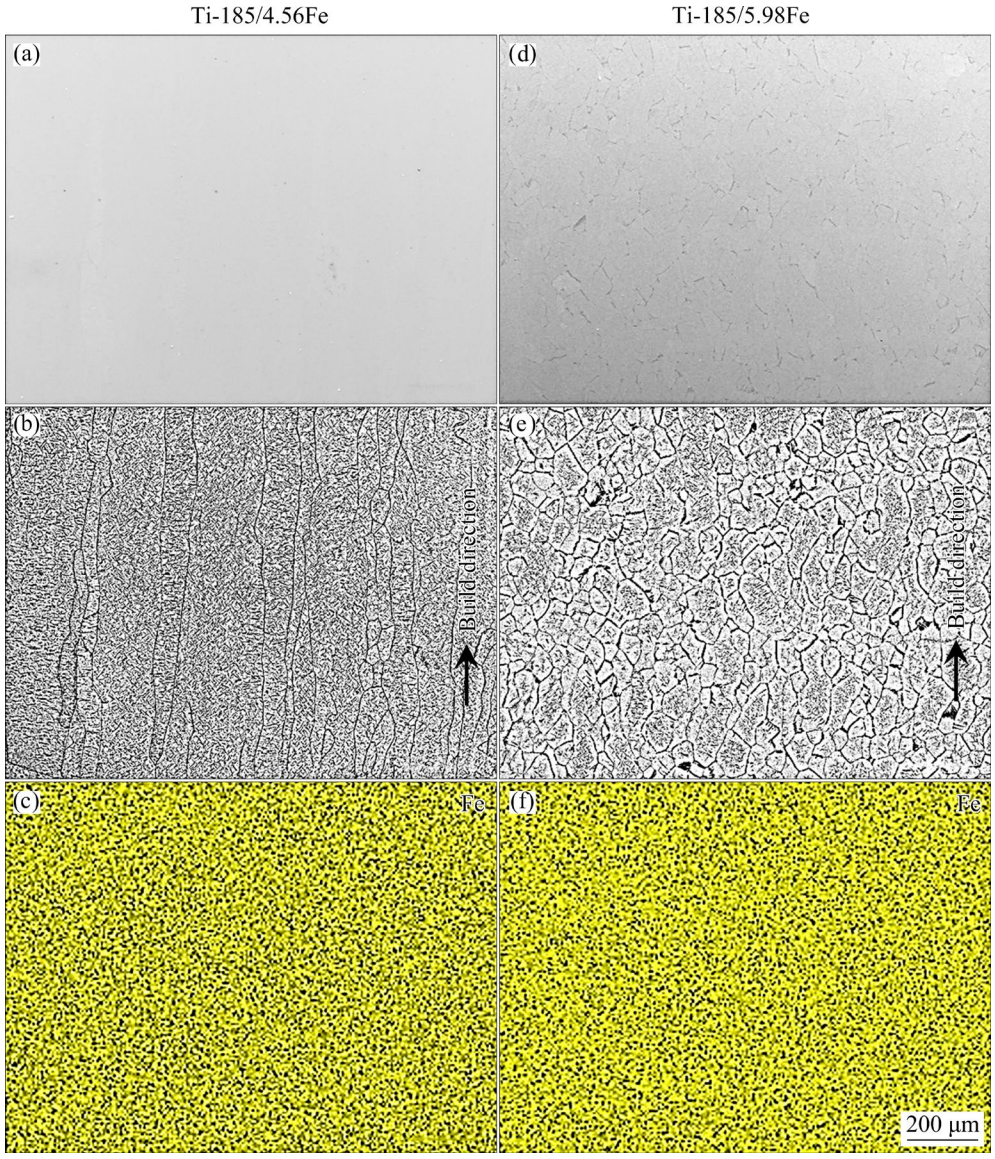

Fig. 3 Microstructures of EB-PBF-printed Ti-185/4.56Fe and Ti-185/5.98Fe alloys: (a, d) Secondary electron images; (b, e) Backscattered electron images; (c, f) SEM−EDS maps of Fe distribution in each microstructure

resulting equiaxed prior-β grains (Fig. 4(d)) is among the finest prior-β grains reported for industrial Ti alloys [18−20] without inoculation or the assistance of an external field.

3.2 In-situ α-phase precipitation

Both grain boundary (GB) and intragranular α-phase precipitates were prevalent in both alloys, as shown in Fig. 5, supporting the XRD results. The GB-α phase is around 1 μm-thick in each alloy but is much less in Ti-185/4.56Fe alloy (Figs. 5(a, b)) than in Ti-185/5.98Fe alloy (Figs. 5(e, f)) due to the differences in the prior-β GB area. The intragranular α phases included microscale primary α-laths (α_p), coarse black phases in Figs. 5(b, f), and nanoscale secondary α-laths (α_s), ultrafine black phases in Figs. 5(b−d, f−h). The latter existed in the remaining β-phase matrix between the α_p-laths (Figs. 5(b, f)). Their formation is due to the confluence of the high powder-bed temperature and the thermal cycling effect.

It is noteworthy that the α_p-laths and α_s-laths are thicker in Ti-185/4.56Fe alloy ((1.01±0.21) μm for α_p-laths and (96.7±20.4) nm for α_s-laths) than in Ti-185/5.98Fe alloy ((0.85±0.22) μm for α_p-laths and (65.8±16.2) nm for α_s-laths). This could be ascribed to the higher $\beta \rightarrow \alpha$ transus temperature of the Ti-185/4.56Fe alloy (lower Fe content), which accelerates diffusion while reducing the strain energy arising from the formation of the α-phase [16].

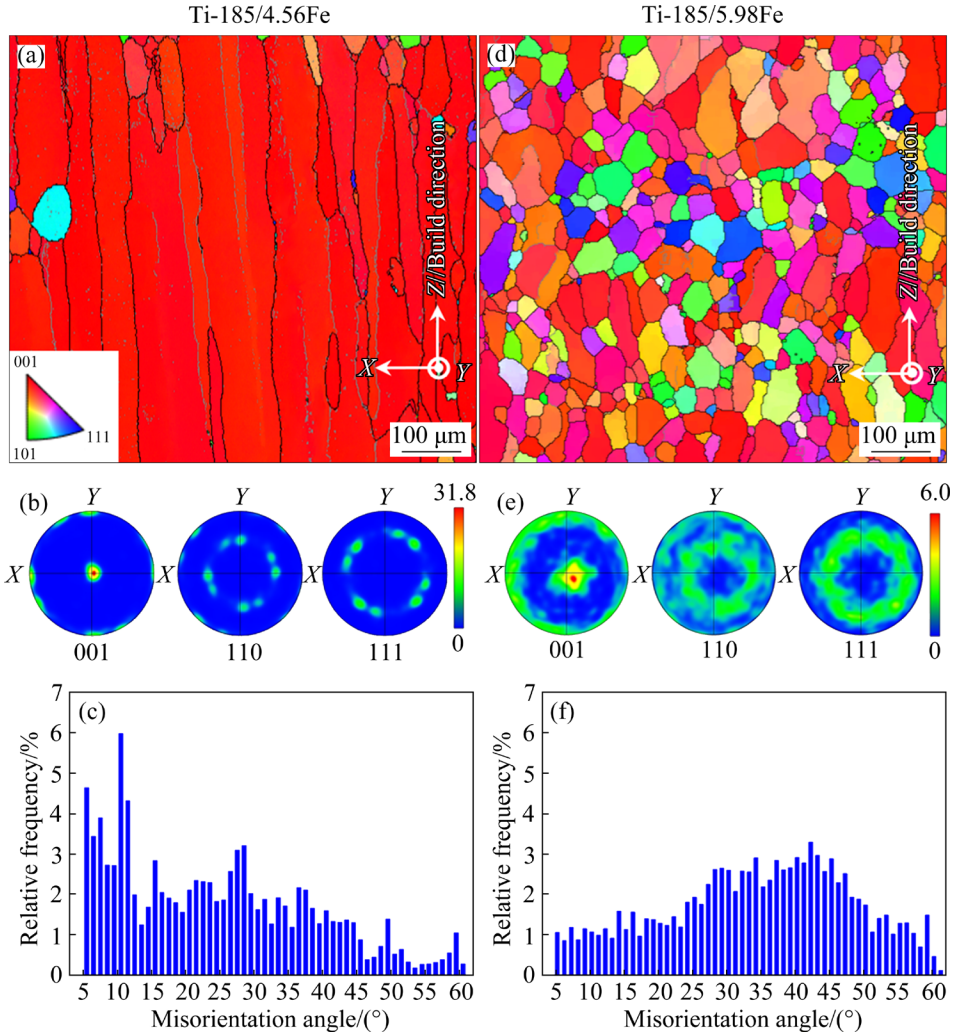

Fig. 4 EBSD analysis results of EB-PBF-printed Ti-185/4.56Fe and Ti-185/5.98Fe alloys along build direction: (a, d) Inverse pole figure maps; (b, e) Pole figures; (c, f) Misorientation angle distribution of prior-β grains

Table 2 lists the TEM−EDS results of each phase in both alloys, measured from three locations. As expected, the Fe content is distinctly different. The α-phase still contains more Al than the β-phase, but the difference is small. This may be attributed to the low bulk Al content in each alloy (1.32%) and the fact that the β-Ti phase can easily dissolve more than 1% Al.

3.3 Tensile properties and fracture features

Figure 6(a) shows the tensile engineering stress−strain (σ−ε) curves obtained from each alloy, while Table 3 summarizes the tensile properties. All tensile samples showed essentially uniform elongation (negligible necking in Fig. 6(b)). As a result, the strength to fracture (σ_f) is almost the same as the ultimate tensile strength (σ_{UTS}) for each alloy (Table 3). The uniform elongation is 4%−6% compared to 2%−4% for AM-fabricated Ti−6Al−4V [21,22]. However, despite its fine equiaxed prior-β grains, the deformation energy of the Ti-185/5.98Fe alloy, $(4.8\pm0.4)\times10^7$ J/m^3, calculated according to $\int_0^{\varepsilon_f}\sigma d\varepsilon$, is much lower (decreased by 30%) than that of the Ti-185/4.56Fe alloy, $(6.2\pm0.1)\times10^7$ J/m^3, due to the decrease in tensile ductility.

The fracture surface features of each alloy, shown in Figs. 7(a−d), correspond well to its prior-β grain structure. For example, Fig. 7(a) mirrors the columnar Ti-185/4.56Fe while Fig. 7(c) echoes the equiaxed Ti-185/5.98. Notably, the feature size in Fig. 7(c) (white dashed contours, (56.2±16.4) μm) coincides with its equiaxed prior-β grain size ((54.2±32.4) μm). Closer inspections revealed lath-like features (yellow dashed lines in Figs. 7(b, d)) among small and shallow dimples. They stem from the fracture of α_p-laths in each alloy. They are

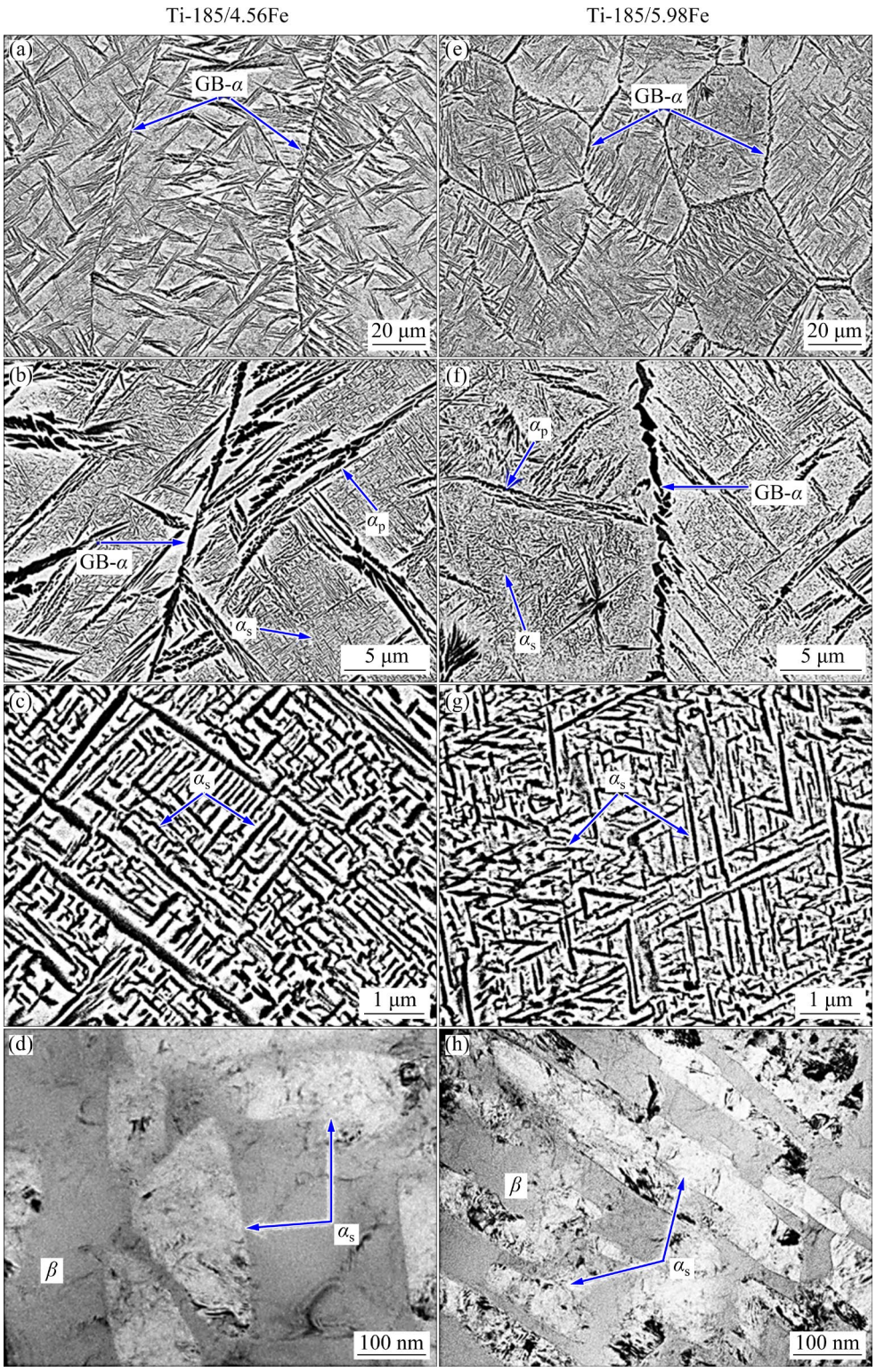

Fig. 5 Microstructures of as-printed Ti-185/4.56Fe and Ti-185/5.98Fe alloys: (a, e) Overview; (b, f) GB-α (coarse black phases), primary α-laths (α_p, black) and secondary α-laths (α_s, ultrafine black phases); (c, g) Closer view of ultrafine α_s-laths (black); (d, h) TEM bright-field images of ultrafine α_s-laths (bright) in remaining β-matrix (grey) between α_p-laths

(0.97±0.34) μm in thickness in Ti-185/4.56Fe (Fig. 7(b)) compared to its α_p-lath thickness of (1.01±0.21) μm (Fig. 5(b)), and (0.81±0.25) μm in thickness in Ti-185/5.98Fe (Fig. 7(d)) versus its α_p-lath thickness of (0.85±0.22) μm (Fig. 5(f)). No signs of fracture of the nanoscale α_s-laths were found.

Table 2 Phase compositions in EB-PBF-printed Ti-185 alloys obtained by TEM−EDS

Alloy	Phase	Content/wt.%			
		Fe	V	Al	Ti
Ti-185/4.56Fe	β	7.47±0.13	10.96±0.18	1.06±0.06	Bal.
	α	0.43±0.09	2.61±0.54	1.70±0.27	Bal.
Ti-185/5.98Fe	β	8.57±1.56	10.20±1.85	1.13±0.16	Bal.
	α	0.98±0.20	3.01±0.62	1.77±0.28	Bal.

To reveal more details of the fracture, areas close to each fracture surface were examined. As shown in Fig. 8, it is found that microcracks are mainly generated via the formation and coalescence of voids in micron-thick GB-α phases, which lead to inter-(prior-β)-granular fracture. These low-solute GB-α phases are weak points in each microstructure. Consequently, the fine equiaxed Ti-185/5.98Fe alloy contained far more weak points

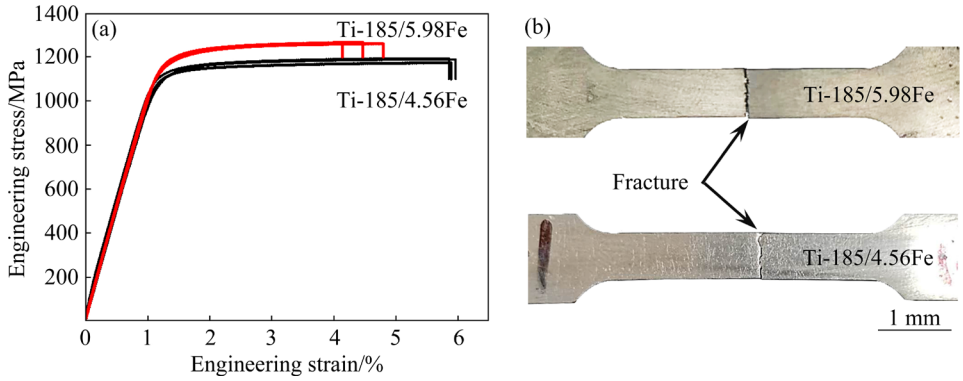

Fig. 6 Comparison of as-printed Ti-185/4.56Fe and Ti-185/5.98Fe alloys: (a) Engineering stress−stain curves; (b) Fractured tensile specimens

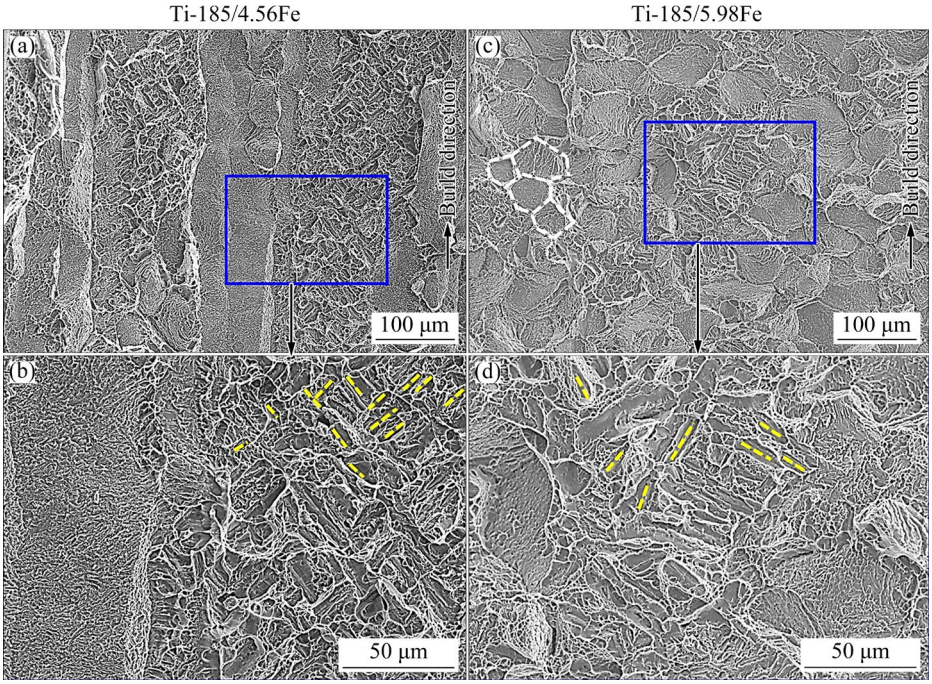

Fig. 7 Comparison of as-printed Ti-185/4.56Fe and Ti-185/5.98Fe alloys: (a) Fracture surface of Ti-185/4.56Fe; (b) Closer view of (a); (c) Fracture surface of Ti-185/5.98Fe; (d) Closer view of (c)

Table 3 Tensile properties of as-printed Ti-185/4.56Fe and Ti-185/5.98Fe alloys

Sample	σ_{UTS}/MPa	$\sigma_{0.2}$/MPa	σ_f/MPa	ε_f/%	ψ_A/%	E/GPa	G/(10^7 J·m^{-3})
Ti-185/4.56Fe (coarse columnar)	1186 ±10	1115±5	1182±11	6.0±0.1	10.7±0.6	99±2	6.2±0.1
Ti-185/5.98Fe (fine equiaxed)	1263±5	1178±11	1262±5	4.6±0.4	7.1±0.3	101±1	4.8±0.4

ψ_A: Reduction in area; E: Elastic modulus; G: Deformation energy = $\int_0^{\varepsilon_f} \sigma d\varepsilon$

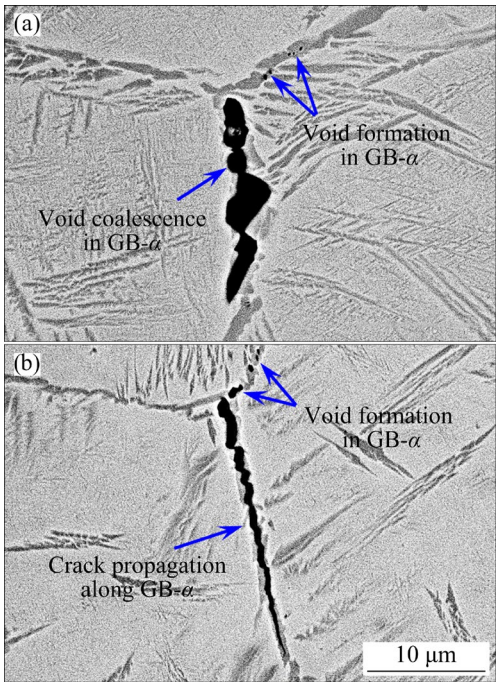

Fig. 8 Formation and coalescence of microvoids in low-solute weak GB-α phases (a) and formation of micro-voids in and microcrack propagation along GB-α phases (b)

(i.e. the GB-α) than the coarse columnar Ti-185/4.56Fe alloy due to its large equiaxed prior-β GB area (Fig. 5). This is due to the pronounced in-situ precipitation of the α-phase along prior-β GBs.

4 Discussion

The above observations clearly indicate that variations in the Fe content of the Ti-185 alloy within the Fe specification range can result in unexpected significant changes in the microstructure during and after solidification when fabricated with EB-PBF, and these variations can lead to highly inconsistent mechanical properties. The underlying reasons and implications are discussed below.

The EB-PBF parameters used in this study (Table 1) were recommended by the system supplier based on their extensive studies on EB-PBF of Ti alloys (wall thickness, build height and orientation). These parameters ensure that virtually pore-free microstructures can be printed with high productivity. Our observations (Fig. 3 and measured densities) fully confirmed that these recommended parameters are essentially the optimal EB-PBF parameters for Ti-185. Under these conditions, increasing the Fe content from 4.56% to 5.98% within the alloy specification range provoked a significant CET (Figs. 3 and 4). In contrast, achieving CET in Ti−6Al−4V via EB-PBF or laser PBF remains a major challenge despite exploring various parameters, including at the expense of density. This work demonstrates an example where varying alloy composition within the specification range (Fe in this study) can be unexpectedly effective in promoting the CET while ensuring a virtually pore-free microstructure.

This Fe-triggered CET can be understood from the enhanced constitutional supercooling (ΔT_{CS}) effect [23]. The ΔT_{CS} is proportional to the solidification range ΔT, where the larger the ΔT, the smaller the grain size in general [23,24]. The true ΔT of an alloy always lies between the Lever rule (ΔT_{Lever}) and the Scheil (ΔT_{Scheil}) predictions. To approach the Lever rule, solute back-diffusion should be on the order of 10^{-9} m^2/s [25]. However, most β-stabilizers including Fe at the solidus temperature have a diffusion coefficient on the order of 10^{-11} m^2/s [25]. Therefore, the true ΔT is closer to ΔT_{Scheil} than ΔT_{Lever}. The ΔT_{Scheil} calculated using the Pandat^{TM} software and PanTi2021 database is 199 °C for Ti-185/4.56Fe and 235 °C for Ti-185/5.98Fe. During the EB-PBF solidification, the smaller ΔT_{CS} of the Ti-185/4.56Fe alloy is inadequate to promote sufficient heterogeneous nucleation or dendrite fragmentation events, thereby allowing columnar growth to continue. In contrast, the solidification of the Ti-185/5.98Fe alloy is featured by a larger ΔT_{CS} due to its higher Fe content, which is in favor of the equiaxed prior-β grain formation through enhanced heterogeneous nucleation or dendrite fragmentation.

It should be noted that in order to achieve an effective CET, suitable solidification conditions must be guaranteed. However, the actual solidification range depends on the solidification cooling conditions, which strongly depend on the selected EB-PBF parameters, including preheating temperature, as well as alloy composition and build geometry. In this regard, the observed CET is best viewed as a result of the combined effects of iron content and appropriate solidification conditions defined by the chosen EB-PBF process.

The improvement in the σ_{UTS} from Ti-185/4.56Fe to Ti-185/5.98Fe registered 77 MPa as seen

in Table 3. Commercially pure Ti Grade 2 has σ_{UTS}=350 MPa (O content <0.25%, Fe content <0.3%) [26], while the binary Ti−6Fe alloy has σ_{UTS}=810 MPa [27]. The corresponding solid solution strengthening effect of Fe (≤6%) is thus about 77 MPa/1 wt.% Fe [27]. Accordingly, the increased σ_{UTS} of the Ti185/5.98Fe alloy can be mainly attributed to the solid solution strengthening of Fe, plus the contribution from the intragranular α-phase precipitates (Fig. 5(f)). However, this mild increase in the σ_{UTS} is accompanied by a significant decrease in tensile deformation energy (Table 3). This is due to two main reasons − the pronounced precipitation of micron-thick GB-α phases and the low strength of these GB-α phases due to their low solute content.

As mentioned above, the solid-solution strengthening effect of Fe (≤6%) in Ti is 77 MPa/1 wt.% Fe [27], while V and Al can add 35 MPa/1 wt.% V and 50 MPa/1 wt.% Al, respectively [27]. According to Table 2, the β-matrix has the composition of Ti−10.20V−8.57Fe−1.13Al in Ti185/5.98Fe. Its strength is thus estimated to be ~1250 MPa, where the strength of high-purity Ti is taken as 200 MPa. The α-phase in this alloy has the composition of Ti−3.01V−0.98Fe−1.77Al (Table 2). The O content in α phase is estimated to be ~0.33% based on: (1) the overall O content (0.13%) in the as-printed Ti-185/5.98Fe alloy, (2) the distribution of O between β and α phases (~0.3, see Supplementary Table 4 of Ref. [16]), and (3) the α-phase volume faction (~0.3, estimated according to the V and Fe contents in β and α in Table 2). The solid strengthening effect of O in Ti is ~100 MPa/0.1 wt% O [28,29]. Therefore, the strength of the α-phase is estimated to be ~800 MPa, which is much lower than the strength of the β-phase (1250 MPa). In other words, the GB-α phases possess weaker microstructural features in these alloys, consistent with the observations shown in Fig. 8. The conclusion is the same for the Ti-185/4.56Fe alloy and other Ti alloys [30].

Under tensile loading conditions, the stress concentration at the interfaces between the GB-α phase and the β-phase matrix increases with increasing applied stress σ [31]. When the applied σ reaches a sufficiently high level (e.g. 0.8σ_{UTS}), microvoids begin to form and coalesce in the micron-thick GB-α phases or at the GB-α/β-matrix interfaces, as shown in Fig. 8. As σ increases further and approaches the level of σ_{UTS}, the local stress intensity factor K ($K \propto \sigma$) reaches the critical value (K_c) of the GB-α phase, leading to inter-prior-β-granular fracture, followed by subsequent fracture through the β-matrix. This weak GB-α phase-facilitated fracture occurred in both alloys as shown in Figs. 7(a, c), where the fracture surface mirrored the prior-β grain structure of each alloy. Furthermore, since the volume fraction of the weak GB-α phase in Ti-185/5.98Fe is much larger than that in Ti-185/4.56Fe, the Ti-185/5.98Fe alloy exhibited a much lower tensile deformation energy.

It is clear from the above discussion that the formation of the weak GB-α phases must be controlled in the as-printed Ti-185 alloy, e.g., by lowering the preheating temperature. However, it is notoriously challenging to suppress GB precipitation. On the other hand, in order to avoid the highly detrimental "powder blowing" phenomena in EB-PBF, it is necessary to keep a sufficiently high powder bed temperature, e.g. above 600 °C for EB-PBF of Ti alloys, which can still easily lead to significant GB-α precipitation in Ti-185. In other words, GB-α is practically unavoidable in EB-PBF-fabricated Ti-185 and similar Ti alloys. Therefore, to ensure good consistency in the as-printed microstructure and mechanical properties, the specification range of Fe for EB-PBF of the Ti-185 alloy should be redefined.

5 Conclusions

(1) Increasing the Fe content from 4.56% to 5.98% in Ti-185 alloy, while still within its Fe specification range, converted coarse columnar prior-β grains (up to 350 μm) into fine equiaxed ones ((54.2±32.4) μm) under the same EB-PBF conditions.

(2) Significant in-situ precipitation of micron-thick low-solute α-phases occurred along each equiaxed prior-β GB. These weak GB α-phases are the main sources of crack initiation sites and propagation pathways.

(3) The tensile deformation energy of the fine equiaxed Ti-185 alloy is 30% lower than that of the coarse columnar Ti-185 alloy due to the prevalence of the weak GB-α phase along each equiaxed prior-β GB.

(4) To ensure good consistency in the as-printed microstructure and mechanical properties,

the specification range of Fe in Ti-185 should be redefined for EB-PBF. Similar observations may occur to the PBF AM of other industrial alloys.

CRediT authorship contribution statement

Quan ZHOU: Data curation, Formal analysis, Investigation, Writing − Original draft, Review and editing; **Xue-zhe ZHANG:** Formal analysis, Investigation, Writing − Review and editing; **Sheng-lu LU:** Investigation, Writing − Review and editing; **Hui-ping TANG:** Supervision, Resources, Writing − Review and editing; **Ma QIAN:** Supervision, Funding acquisition, Writing − Original draft, Review and editing.

Declaration of competing interest

The authors declare that they have no known competing financial interests or personal relationships that could have appeared to influence the work reported in this paper.

Acknowledgments

This work was supported by the National Natural Science Foundation of China (No. 51829401), and the Australian Research Council (No. DP220103407).

References

[1] GROSS J R, MOORHEAD P E, ABKOWITZ S. Titanium base aluminum−vanadium−iron alloys: US Patent, 2819959A [P]. 1958−01−14.

[2] BOYER R, WELSCH G, COLLINGS E W. Materials properties handbook: Titanium alloys [M]. Ohio: ASM International, 1994.

[3] DEVARAJ A, JOSHI V V, SRIVASTAVA A, MANANDHAR S, MOXSON V, DUZ V A, LAVENDER C. A low-cost hierarchical nanostructured beta-titanium alloy with high strength [J]. Nature Communications, 2016, 7: 11176.

[4] MITCHELL A, KAWAKAMI A, COCKCROFT S L. Segregation in titanium alloy ingots [J]. High Temperature Materials and Processes, 2007, 26: 59−77.

[5] ZENG W D, ZHOU Y G. Effect of beta flecks on mechanical properties of Ti−10V−2Fe−3Al alloy [J]. Materials Science and Engineering: A, 1999, 260: 203−211.

[6] ZHOU Q, ZHANG X Z, TANG H P, QIAN M. Electron beam additively manufactured Ti−1Al−8V−5Fe alloy: In situ precipitation hardening, tensile properties and fracture characteristics [J]. Materials Science and Engineering: A, 2023, 865: 144639.

[7] YAO X X, LI J Y, WANG Y F, GAO X, ZHANG Z. Numerical simulation of powder effect on solidification in directed energy deposition additive manufacturing [J]. Transactions of Nonferrous Metals Society of China, 2021, 31: 2871−2884.

[8] ZHOU Q, ZHANG X Z, SONG T, LU S L, DONG T, TANG H P, QIAN M. Laser directed energy deposition of Ti−1Al−8V−5Fe alloy: From zero to significant tensile plasticity [J]. Scripta Materialia, 2024, 239: 115814.

[9] MEHJABEEN A, XU W, QIU D, QIAN M. Redefining the β-phase stability in Ti−Nb−Zr alloys for alloy design and microstructural prediction [J]. JOM, 2018, 70: 2254−2259.

[10] COLLINS P C, BANERJEE R, BANERJEE S, FRASER H L. Laser deposition of compositionally graded titanium–vanadium and titanium–molybdenum alloys [J]. Materials Science and Engineering: A, 2003, 352: 118−128.

[11] BERMINGHAM M J, MCDONALD S D, DARGUSCH M S, STJOHN D H. Grain-refinement mechanisms in titanium alloys [J]. Journal of Materials Research, 2008, 23: 97−104.

[12] WANG X, ZHANG L J, NING J, LI S, ZHANG L L, LONG J, MA W. Fe element promotes the transformation from columnar to equiaxed grains and the formation of ultrafine microstructure of Ti−6Al−4V alloy by laser wire deposition [J]. Additive Manufacturing, 2021, 48: 102442.

[13] WANG H, LUO H L, CHEN J Q, TANG J C, YAO X Y, ZHOU Y H, YAN M. Cost-affordable, biomedical Ti−5Fe alloy developed using elemental powders and laser in-situ alloying additive manufacturing [J]. Materials Characterization, 2021, 182: 111526.

[14] SIMONELLI M, MCCARTNEY D G, BARRIOBERO-VILA P, ABOULKHAIR N T, TSE Y Y, CLARE A, HAGUE R. The influence of iron in minimizing the microstructural anisotropy of Ti−6Al−4V produced by laser powder-bed fusion [J]. Metallurgical and Materials Transactions A, 2020, 51: 2444−2459.

[15] AL-BERMANI S S, BLACKMORE M L, ZHANG W, TODD I. The origin of microstructural diversity, texture, and mechanical properties in electron beam melted Ti−6Al−4V [J]. Metallurgical and Materials Transactions A, 2010, 41: 3422−3434.

[16] SONG T, CHEN Z, CUI X, LU S, CHEN H, WANG H, DONG T, QIN B, CHAN K C, BRANDT M, LIAO X, RINGER S P, QIAN M. Strong and ductile titanium–oxygen–iron alloys by additive manufacturing [J]. Nature, 2023, 618: 63−68.

[17] WELK B A, TAYLOR N, KLOENNE Z, CHAPUT K J, FOX S, FRASER H L. Use of alloying to effect an equiaxed microstructure in additive manufacturing and subsequent heat treatment of high-strength titanium alloys [J]. Metallurgical and Materials Transactions A, 2021, 52: 5367−5380.

[18] LIU T Y, MIN X H, ZHANG S, WANG C S, DONG C. Microstructures and mechanical properties of Ti−Al−V−Nb alloys with cluster formula manufactured by laser additive manufacturing [J]. Transactions of Nonferrous Metals Society of China, 2021, 31: 3012−3023.

[19] WANG H, MA S Y, WANG J C, LU T, LIU C M. Microstructure and mechanical properties of TA15/TC11 graded structural material by wire arc additive manufacturing process [J]. Transactions of Nonferrous Metals Society of China, 2021, 31: 2323−2335.

[20] YAN W G, WANG H M, TANG H B, CHENG X, ZHU Y Y. Effect of Nd addition on microstructure and tensile properties of laser additive manufactured TC11 titanium alloy [J]. Transactions of Nonferrous Metals Society of

China, 2022, 32: 1501−1512.
[21] TODARO C J, EASTON M A, QIU D, ZHANG D, BERMINGHAM M J, LUI E W, BRANDT M, STJOHN D H, QIAN M. Grain structure control during metal 3D printing by high-intensity ultrasound [J]. Nature Communications, 2020, 11: 142.
[22] CARROLL B E, PALMER T A, BEESE A M. Anisotropic tensile behavior of Ti−6Al−4V components fabricated with directed energy deposition additive manufacturing [J]. Acta Materialia, 2015, 87: 309−320.
[23] TARSHIS L A, WALKER J L, RUTTER J W. Experiments on the solidification structure of alloy castings [J]. Metallurgical Transactions, 1971, 2: 2589−2597.
[24] NARTU M S K K Y, WELK B A, MANTRI S A, TAYLOR N L, VISWANATHAN G B, DAHOTRE N B, BANERJEE R, FRASER H L. Underlying factors determining grain morphologies in high-strength titanium alloys processed by additive manufacturing [J]. Nature Communications, 2023, 14: 3288.
[25] LIU H, LIU Y, LU S L, ZHANG Y, CHEN H, CHEN Y, QIAN M. Alloy solidification: Assessment and improvement of an easy-to-apply model [J]. Journal of Materials Science & Technology, 2022, 130: 1−11.
[26] POLMEAR I J, STJOHN D, NIE J E, QIAN M. Light alloys: Metallurgy of the light metals [M]. 5th ed. Oxford: Butterworth-Heinemann, 2017.
[27] MOISEYEV V N. Titanium alloys: Russian aircraft and aerospace applications [M]. Boca Raton: CRC Press, 2006.
[28] LUO S D, SONG T, LU S L, LIU B, TIAN J, QIAN M. High oxygen-content titanium and titanium alloys made from powder [J]. Journal of Alloys and Compounds, 2020, 836: 155526.
[29] XIA Y, ZHAO J L, TIAN Q H, GUO X Y. Review of the effect of oxygen on titanium and deoxygenation technologies for recycling of titanium metal [J]. JOM, 2019, 71: 3209−3220.
[30] LÜTJERING G, WILLIAMS J C. Titanium [M]. 2nd ed. Berlin: Springer, 2007.
[31] HULL D, BACON D J. Introduction to dislocations [M]. 5th ed. Oxford: Butterworth-Heinemann, 2011.

电子束增材制造不同铁含量 Ti−1Al−8V−5Fe 合金的显微组织及力学性能

周 全[1,2,3]，张学哲[2]，Sheng-lu LU[3]，汤慧萍[2,4]，Ma QIAN[3]

1. 东北大学 材料科学与工程学院，沈阳 110819；
2. 西北有色金属研究院 金属多孔材料国家重点实验室，西安 710016；
3. Centre for Additive Manufacturing, School of Engineering, RMIT University, Melbourne, Victoria 3000, Australia;
4. 浙大城市学院 先进材料增材制造创新研究中心，杭州 310015

摘 要：利用电子束粉末床熔融增材制造技术制备不同铁含量 Ti−1Al−8V−5Fe (Ti-185)合金，并研究其显微组织和力学性能。结果表明，当粉末铁含量从 4.56%(质量分数)增加到 5.98%(质量分数)时(成分仍在规定范围内)，打印态合金的原始 β 晶粒由粗大柱状晶粒转变为细小等轴晶粒((54.2±32.4) μm)。然而，由于随后打印过程中的原位沉淀析出，等轴晶的晶界处析出大量连续、低溶质含量的 α 相。虽然强度略有增加，但是相对应的拉伸变形能从粗晶的 6.2×10^7 J/m^3 急剧降低到等轴晶的 4.8×10^7 J/m^3。合金断裂特性表明，这些晶界 α 相是裂纹萌生和扩展的主要位置。

关键词：Ti−1Al−8V−5Fe 合金；等轴晶；变形能；晶界 α；相析出

(Edited by Wei-ping CHEN)